Nano Research

ISSN 1998-0124 CN 11-5974/O4
https://doi.org/10.1007/s12274-020-3193-y

Research Article

Raman scattering investigation of twisted WS_2/MoS_2 heterostructures: interlayer mechanical coupling versus charge transfer

Lishu Wu[1,§], Chunxiao Cong[2,§] (✉), Jingzhi Shang[3] (✉), Weihuang Yang[4], Yu Chen[1], Jiadong Zhou[5], Wei Ai[3], Yanlong Wang[6], Shun Feng[1], Hongbo Zhang[1], Zheng Liu[5], and Ting Yu[1] (✉)

[1] *Division of Physics and Applied Physics, School of Physical and Mathematical Sciences, Nanyang Technological University, Singapore 637371, Singapore*
[2] *School of Information Science and Technology, Fudan University, Shanghai 200433, China*
[3] *Shaanxi Institute of Flexible Electronics, Northwestern Polytechnical University, Xi'an 710129, China*
[4] *Engineering Research Center of Smart Microsensors and Microsystems, Ministry of Education, College of Electronics and Information, Hangzhou Dianzi University, Hangzhou 310018, China*
[5] *School of Materials Science and Engineering, Nanyang Technological University, Singapore 639798, Singapore*
[6] *Key Laboratory of Chemical Lasers, Dalian Institute of Chemical Physics, Chinese Academy of Sciences, Dalian 116023, China*
[§] *Lishu Wu and Chunxiao Cong contributed equally to this work.*

Received: 19 August 2020 / Revised: 9 October 2020 / Accepted: 15 October 2020

ABSTRACT

Twisted van der Waals homo- and hetero-structures have aroused great attentions due to their unique physical properties, providing a new platform to explore the novel two-dimensional (2D) condensed matter physics. The robust dependence of phonon vibrations and electronic band structures on the twist angle has been intensively observed in transition metal dichalcogenide (TMD) homo-structures. However, the effects of twist angle on the lattice vibrational properties in the TMD heterostructures have not caused enough attention. Here, we report the distinct evolutions of Raman scattering and the underlying interlayer interactions in the twisted WS_2/MoS_2 heterostructures. The shifts and linewidths of $E_{2g}(\Gamma)$ and $A_{1g}(\Gamma)$ phonon modes are found to be twist angle dependent. In particular, analogous to that of the twisted TMD homostructures, the frequency separations between $E_{2g}(\Gamma)$ and $A_{1g}(\Gamma)$ modes of MoS_2 and WS_2 in the twisted heterostructures varying with twist angle correlate with the interlayer mechanical coupling, essentially originating from the spacing-related repulsion between sulfur atoms. Moreover, the opposite shift behaviors and broadening of $A_{1g}(\Gamma)$ modes caused by charge transfer are also observed in the twisted heterostructures. The calculated interlayer distances and band alignment of twisted WS_2/MoS_2 through density functional theory further evidence our interpretations on the roles of the interlayer mechanical coupling and charge transfer in variations of Raman features. Such understanding and controlling of interlayer interaction through the stacking orientation are significant for future optoelectronic device design based on the newly emerged 2D heterostructures.

KEYWORDS

van der Waals heterostructures, interlayer coupling, Raman scattering, twist angle, charge transfer

1 Introduction

The rising van der Waals (vdWs) homo- and hetero-structures consisting of the same or different kinds of two-dimensional (2D) layers, have attracted tremendous interests due to their intriguing properties and extraordinary device performances [1–3]. Such homo- and hetero-structures can be fabricated through transfer and chemical vapor deposition (CVD) methods [4–6]. For example, heterostructures of Sb_2O_3/WS_2 and SnS_2/MoS_2 have been successfully prepared by selective and direct CVD growth techniques [4, 5]. Specifically, the dangling-bond-free layered structure and the improvement of growth, exfoliation, and transfer techniques of 2D materials makes it allowable to explore more unique optical properties in the vdWs homo- and hetero-structures with high quality through either selecting the materials of 2D layers or tuning the stacking orientation between the layers. The vdWs homo- and hetero-structures are offering a new platform to study the novel physics and develop potential applications. For example, it has been reported that the quantum yield of monolayer transition metal dichalcogenides (TMDs) can be enhanced up to 10% in multiple quantum wells (MQWs) with the structure unit of graphene/h-BN/TMDs [7]. The novel transport such as unconventional superconductivity and optical properties of moiré exciton are recently discovered in moiré twisted vdWs homo-and hetero-structures, which are attributed to the modulation of electronic band structures by the moiré superlattice [8–11]. Recent studies on interlayer coupling of vertically stacked TMD homo-structures and hetero-structures, i.e., MX_2/MX_2 and $MX_2/M'X'_2$ (M and M' are Mo or W; X and X' stand for S, Se, or Te) have attracted a great deal of attention [12–15]. For the homo-structures of TMDs, the interlayer interaction with respect to the interlayer stacking has been thoroughly explored [16–20], in which not only the phonon vibrational properties but also the band

Address correspondence to Chunxiao Cong, cxcong@fudan.edu.cn; Jingzhi Shang, iamjzshang@nwpu.edu.cn; Ting Yu, yuting@ntu.edu.sg

structures show the twist angle-dependent variation behaviors. For the hetero-structures of TMDs, various interlayer coupling phenomena have been observed in MoS_2/WS_2 [21–24], WSe_2/WS_2 [25, 26], $MoS_2/MoSe_2$ [27], MoS_2/WSe_2 [12], $MoSe_2/WS_2$ [22], and $WSe_2/MoSe_2$ [28–31], such as strong photoluminescence (PL) quenching effect, interlayer exciton formation, ultrafast charge separation, etc. However, twist angle-dependent phonon vibrational properties remain largely unexplored in the TMD hetero-structures which are crucial to understand the interlayer mechanical coupling and the band alignment of TMD hetero-structures. Here, in this work, we have performed the systematic Raman measurements on twisted WS_2/MoS_2 heterostructures. The interplays of interlayer mechanical coupling and charge transfer on phonon vibrational features have been associated with the observed periodic modulations of fingerprinting Raman modes. Understanding of interlayer interactions of such artificially formed vdWs structures is fundamentally important and provides new insights into manipulating the performances of potential devices.

2 Results and discussion

The WS_2/MoS_2 heterostructures with various twist angles were fabricated via a dry-transfer method [6] in combination with the home-made transfer set-up (See Fig. 1(a) and Methods). Monolayer MoS_2 and WS_2 were first grown through the CVD method [32, 33]. Then, the optical contrast and fluorescence imaging techniques were used to identify the monolayer samples [32, 34, 35]. To transfer monolayer WS_2 from the substrate to the polydimethylsiloxane (PDMS) polymer film pre-deposited on the glass, a dry transfer technique was used. As most of the monolayer samples are triangular, a batch of the twisted WS_2/MoS_2 heterostructures could be obtained through properly rotating the samples by means of the optical microscopic system equipped with the micromanipulator (shown in Fig. 1(a)). Figure 1(b) shows the schematic of side views of AA (i.e., 3R) and AB (i.e., 2H) stacking orders of WS_2/MoS_2 heterostructures. Figure 1(c) depicts the schematic of triangular monolayer MoS_2 and WS_2 with sulfur-terminated zigzag (S-zz) edges. Blue

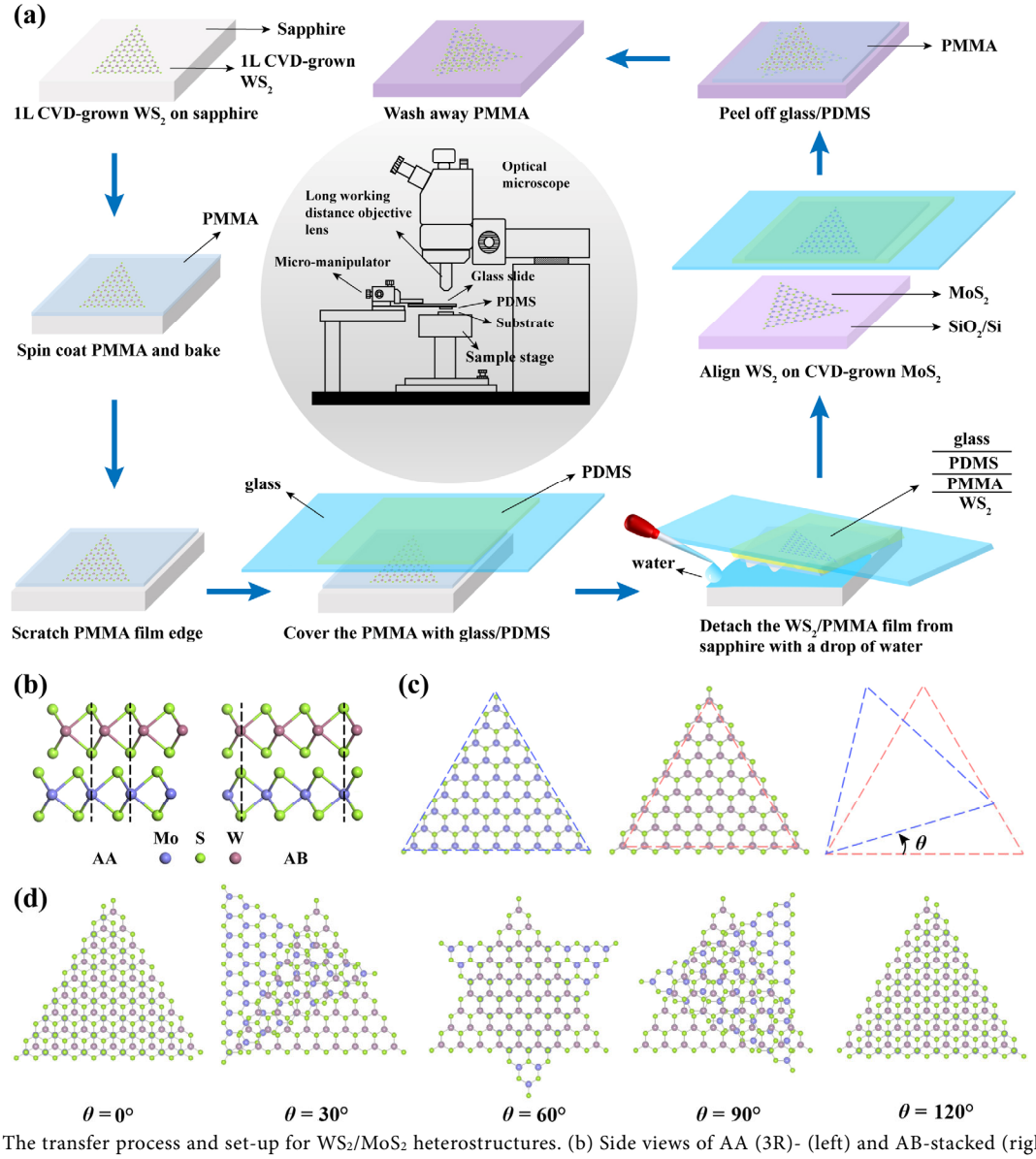

Figure 1 (a) The transfer process and set-up for WS_2/MoS_2 heterostructures. (b) Side views of AA (3R)- (left) and AB-stacked (right) WS_2/MoS_2 heterostructures, where Mo, S, and W atoms are represented by purple, green, and pink balls, respectively. The black dashed lines show the superpositions of metal and S atoms in different layers. (c) The determination of the twist angle θ. The twist angle is defined as the angle that the top WS_2 layer rotates counterclockwise around the triangle apex to match the orientation of the bottom MoS_2 layer. Blue and red triangles indicate the bottom MoS_2 layer and the top WS_2 layer, respectively. (d) Schematics of the heterostructure configurations when θ equals to 0°, 30°, 60°, 90°, and 120°. The 120° case is identical to 0°. Note that, the triangles used for the twist angle definition all have sulfur-terminated zigzag (S-zz) edges.

and red dashed triangles represent bottom MoS_2 and top WS_2 monolayers, respectively. As the two triangles possess the same edges, the twist angle θ in this paper can be defined as the angle that the top WS_2 layer rotates counterclockwise around the triangle apex to match the orientation of the bottom MoS_2 layer. For instance, the AB-stacked heterostructures have a twist angle of 60°, where the S (W) atoms of top WS_2 sit right above the Mo (S) atoms of bottom MoS_2 (See Figs. 1(b) and 1(d)). The top-view schematics of the rest twisted WS_2/MoS_2 heterostructures with specific θ of 0°, 30°, 90°, and 120° are also illustrated in Fig. 1(d). Note that owing to the periodic twist, the stacking configuration of $\theta = 120°$ is identical to $\theta = 0°$. However, in real cases, besides the S-zz edge, the Mo-zz edge is another most energetically favorable edge orientation. Thus, to identify θ, the initial value of θ between MoS_2 and WS_2 triangles was first observed through the optical microscope; then, the method developed by van der Zande et al. [36] was used to further determine the edge profiles of MoS_2 and WS_2 monolayer triangles. If the edge types of MoS_2 and WS_2 are different, i.e., one belongs to S-zz, and the other is Mo-zz, additional 60° should be added into the final value of θ. The uncertainty of the determined θ is less than 2°.

To systematically probe the optical properties of the twisted WS_2/MoS_2 heterostructures, Raman and PL measurements have been performed with a WITec confocal Raman system [34, 37, 38]. All tests were done at room temperature using a 532 nm laser with the power within 100 μW, unless otherwise stated. The Raman spectra are normalized to the Si peak located at 520 cm^{-1} (See details in Methods). Figure 2(a) shows the optical image of WS_2/MoS_2 heterostructure with θ equal to 23°, where monolayer WS_2 and MoS_2 were enclosed by the white and black dashed curves, respectively. Figure 2(b) exhibits the typical schematic of type-II band alignment in the WS_2/MoS_2 heterostructure, which has been reported previously [21, 39, 40]. The room-temperature PL spectra of pristine monolayer MoS_2, WS_2/MoS_2 heterostructure, and pristine monolayer WS_2 are shown in Fig. 2(c), which are represented by blue, pink, and grey dot points, respectively. The corresponding colored solid lines are the Lorentzian fitting curves. For pristine monolayer MoS_2, two prominent peaks were observed at around 1.83 and 1.99 eV, which are assigned to negatively charged A exciton (X_A^-) and neutral B exciton (X_B) [41, 42], respectively. In addition, the negatively charged (X_A^-) and neutral A excitons (X_A) located at 1.98 and 2.02 eV [32, 34, 43, 44], separately, were found to dominate the PL spectrum of pristine monolayer WS_2. In contrast, the WS_2/MoS_2 heterostructure demonstrates a distinctive luminescence emission feature appearing between the X_A^- of pristine MoS_2 and WS_2 monolayers. The emission feature can be well fitted by a symmetric peak with the extracted position of 1.89 eV using Lorentzian function. To unravel the underlying origins, we first take the interlayer interaction associated with charge transfer into consideration. As presented in Fig. 2(b), a typical band alignment of type-II is formed in WS_2/MoS_2 heterostructures, where the hole (electron) can transfer from MoS_2 (WS_2) to WS_2 (MoS_2). Hence, the emissions of X_A^- of MoS_2; X_A^- and X_A of WS_2 enabled by the radiative recombination of active electrons with holes were quenched due to the charge transfer [21, 24, 28, 45]. Furthermore, as the electron is accumulated at the conduction band of MoS_2, some alternative band transitions

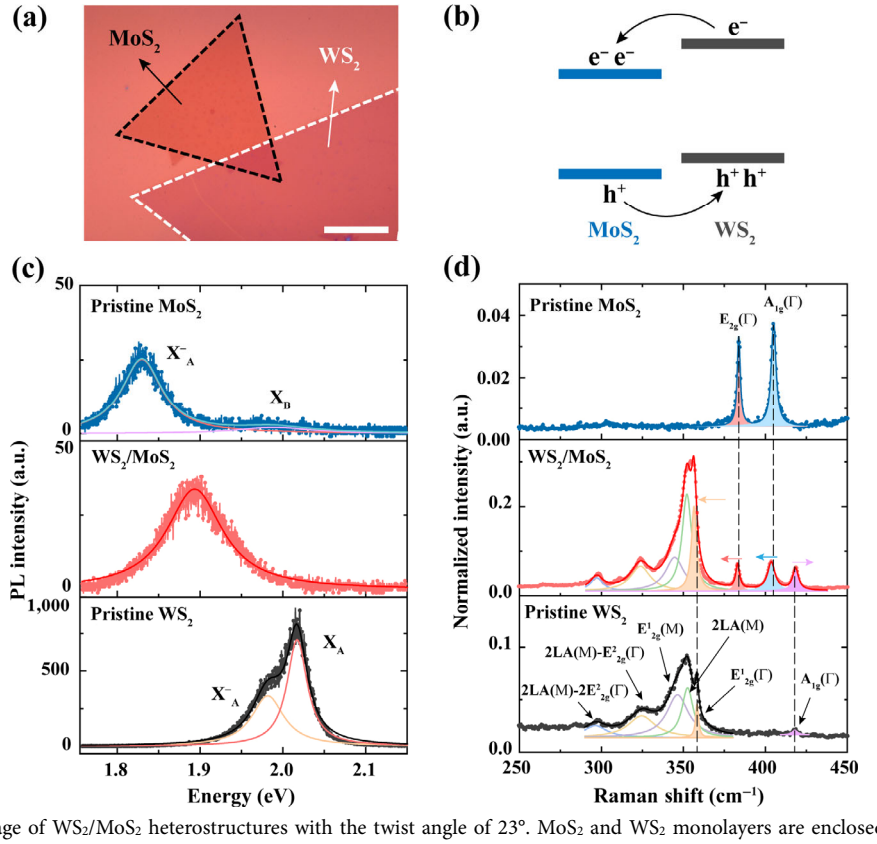

Figure 2 (a) Optical image of WS_2/MoS_2 heterostructures with the twist angle of 23°. MoS_2 and WS_2 monolayers are enclosed by the black and white dashed curves, respectively. Scale bar: 15 μm. (b) Schematic of the staggered band alignment in the heterostructure, where the black arrows represent the electron (hole) transfers from WS_2 (MoS_2) to MoS_2 (WS_2). (c) PL and (d) Raman spectra of pristine monolayer MoS_2 and WS_2, and WS_2/MoS_2 heterostructures at room temperature. The blue, pink, and grey dot points are the experimental data of pure MoS_2, WS_2/MoS_2, and pure WS_2, separately. The corresponding colored solid lines show the fit curves as a result of multiple peak fit with Lorentzian function. The phonon modes of $E_{2g}(\Gamma)$ and $A_{1g}(\Gamma)$ mainly discussed in the main text are labeled aside the fitted peaks with shadows and the corresponding colored arrows point out the peak shift directions in the heterostructures. The black straight dashed lines in (d) mark the original peak positions in the constituent layers.

can also possibly happen, like spatially indirect exciton band transition (interlayer exciton) [46, 47]. However, the interlayer exciton energy of WS_2/MoS_2 heterostructures is roughly around 1.4 eV [48, 49], far beyond 1.89 eV discovered in our case. Therefore, in line with the previous studies [41, 44, 50, 51] of excitons in monolayer TMDs, we assign the dominated peak of 1.89 eV in the PL spectrum of the heterostructures to the possible neutral A exciton of monolayer MoS_2 instead. Figure 2(d) also exhibits Raman spectra of pristine MoS_2 and WS_2, and WS_2/MoS_2 heterostructure over the frequency range of 250–450 cm^{-1} at room temperature, which are represented by blue, grey, and pink dot points, respectively. The corresponding colored solid lines show the Lorentzian fit curves. The typical phonon modes of E_{2g} and A_{1g} at the Γ point with frequency separations of 21.2 and 59.8 cm^{-1} were evidently observed in pristine MoS_2 and WS_2, respectively, which confirms the monolayer nature of pristine MoS_2 and WS_2 [20, 32, 36]. For the case of WS_2, the rest of Raman modes, like 2LA(M), are found and also labeled, as indicated in the bottom panel of Fig. 2(d). In comparison with pristine MoS_2 and WS_2, the Raman features of WS_2/MoS_2 heterostructure displays particular variations. As seen in the middle panel of Fig. 2(d), first, the intensity of $A_{1g}(\Gamma)$ mode of WS_2 in the heterostructure is increased by ~ 9 times, compared to that of pristine WS_2 and the increasing is also observed to vary with the twist angle θ (for details, see Fig. S1 in the Electronic Supplementary Material (ESM)). Second, both $E_{2g}(\Gamma)$ modes of MoS_2 and WS_2 along with the $A_{1g}(\Gamma)$ mode of MoS_2 soften, while the $A_{1g}(\Gamma)$ mode of WS_2 stiffens. After further examining the evolution of $E_{2g}(\Gamma)$ and $A_{1g}(\Gamma)$ phonon modes with different twist angles in the heterostructures (Fig. 3(a)), we found that the softening and stiffening can be tunable with the twist angle θ. The similar phenomena have been also found in twisted TMD homostructures [16–19]. When θ is around 0°, 60° or 120°, the $E_{2g}(\Gamma)$ modes of WS_2 and MoS_2 were softened by up to 2 and 0.6 cm^{-1}, respectively (See Figs. 3(b) and 3(c)); whereas the $A_{1g}(\Gamma)$ modes around 30° or 90° were softened by up to 1.5 cm^{-1} and stiffened by about 0.7 cm^{-1}, for MoS_2 and WS_2, separately (See Figs. 3(d) and 3(e)). Note that although the overtone and combination modes originating from the Brillouin zone center and zone edge phonons of WS_2 may also differ, we do not discuss them in this work, as they can be affected by many factors [52, 53], which are beyond our scope of this work.

To explain the origins behind the phenomena, we first consider the effects on the frequencies of the $E_{2g}(\Gamma)$ and $A_{1g}(\Gamma)$ phonon modes. Previous Raman studies suggest that the tensile strain and the enhanced dielectric screening can soften the $E_{2g}(\Gamma)$ mode [18, 19, 52–56]. In our case, as the $E_{2g}(\Gamma)$ modes of WS_2 and MoS_2 were not split and broadened (See Fig. S2 in the ESM), we attribute the identical redshifts of the two $E_{2g}(\Gamma)$

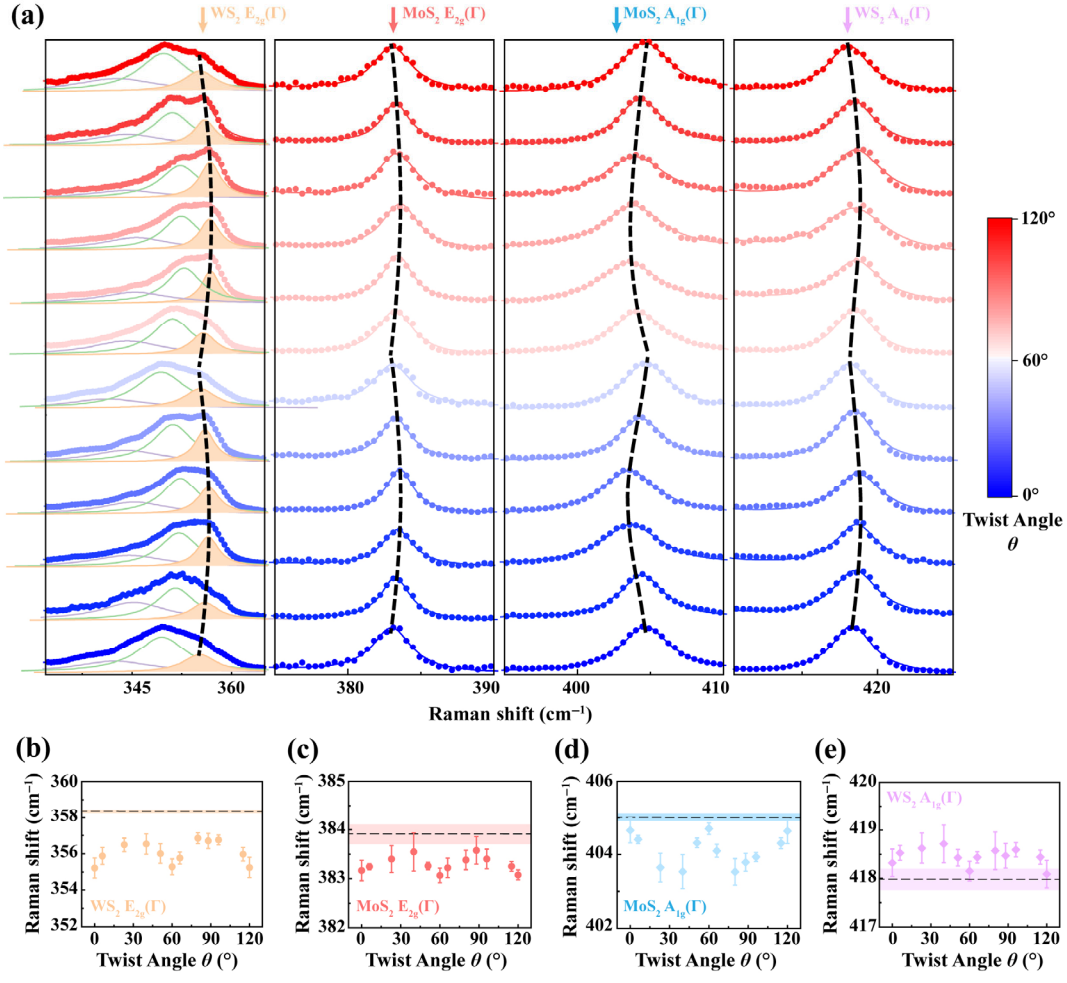

Figure 3 (a) Tuning of the $E_{2g}(\Gamma)$ and $A_{1g}(\Gamma)$ phonon modes in the heterostructures with twist angle θ. The color bar from blue to red represents the twist angle ranging from 0° to 120°. The dots are experimental data points, while the corresponding solid curves are Lorentzian fitting to the data. The black dash lines showing the relevant tuning trends are guided for eyes. All of the spectra are normalized and offset. For better clarity, the $E_{2g}(\Gamma)$ peaks of WS_2 are filled with the light orange shadows. The θ dependence of the frequencies of (b) WS_2 $E_{2g}(\Gamma)$, (c) MoS_2 $E_{2g}(\Gamma)$, (d)MoS_2 $A_{1g}(\Gamma)$, and (e) WS_2 $A_{1g}(\Gamma)$ phonon modes. The error bars plotted together are obtained from the fitting and statistics. The horizontal dashed lines and the shaded areas represent the average value and standard deviation of the initial peak positions of $E_{2g}(\Gamma)$ and $A_{1g}(\Gamma)$ of pristine monolayer MoS_2 and WS_2, respectively.

modes of the heterostructures to the enhanced dielectric screening [54, 55, 57]. For the $A_{1g}(\Gamma)$ phonon mode, it has been reported that it can be responsive to both interlayer coupling dependent on the layer number and carrier doping [19, 58, 59]. The interlayer coupling stiffens the $A_{1g}(\Gamma)$ as the layer number increases, whereas the carrier doping softens the $A_{1g}(\Gamma)$ as the electron density increases. In WS_2/MoS_2 heterostructures, the interlayer mechanical coupling stiffens the $A_{1g}(\Gamma)$ modes for both materials; whereas due to the unidirectional electron transfer from WS_2 to MoS_2, the increased electron density in MoS_2 and the reduced electron density in WS_2 can also soften and stiffen the $A_{1g}(\Gamma)$ modes, respectively. Thus, the remarkably opposite shifts of the two $A_{1g}(\Gamma)$ modes in the heterostructures are ascribed to the combinational effects of interlayer coupling and charge transfer-induced doping in WS_2 and MoS_2 layers. On the other hand, the tuning behaviors of $E_{2g}(\Gamma)$ and $A_{1g}(\Gamma)$ with the twist angle θ reveal that the evolution of interlayer mechanical coupling in the twisted TMD heterostructures is also possible, analogous to twisted TMD homostructures.

In line with the previous studies of twisted TMD homostructures [16–19], the frequency separation between the $E_{2g}(\Gamma)$ and $A_{1g}(\Gamma)$ phonon modes ($\omega_A - \omega_E$) characterizes the effective interlayer mechanical coupling strength. The larger frequency separation indicates the stronger interlayer mechanical coupling. Therefore, we calculated the frequency differences ($\omega_A - \omega_E$) of MoS_2 and WS_2 as shown in Figs. 4(a) and 4(b), using the extracted peak positions in Figs. 3(b)–3(e). The error bars are derived from the equation of propagation of uncertainty (See the ESM). It can be seen that the separations ($\omega_A - \omega_E$) of MoS_2 and WS_2 in the heterostructures display the similar periodic variations, but with different symmetric downshifts of 2 and 1 cm^{-1}, respectively. Interestingly, after the theoretical calculations of interlayer distances of twisted WS_2/MoS_2 heterostructures, it was found that the pattern of the variations of the interlayer distances with the twist angle θ is analogous to that of the separations. Specifically, under θ = 0°, 38.3° and 60° configurations (See Fig. 4(c)), the interlayer distances have been estimated as 5.806, 6.576, and 5.838 Å, respectively (Fig. 4(d)), which implies that the interlayer spacing of 0° and 60° is comparable to each other, but dramatically smaller than that of 38.3°, thus the WS_2/MoS_2 heterostructures with the twist angle equal to 0° and 60° are more like "bilayer" structures in connection with the stronger interlayer mechanical coupling. In that case, the separations ($\omega_A - \omega_E$) around 0° or 60° turn out to be larger, whereas smaller for θ around 30° or 90°, which is consistent with the observation in Figs. 4(a) and 4(b). Combining the experimental results and density functional theory (DFT) calculations, we conclude that analogous to twisted TMD homostructures, the frequency separation between the $E_{2g}(\Gamma)$ and $A_{1g}(\Gamma)$ phonon modes ($\omega_A - \omega_E$) is also capable of the characterization of interlayer mechanical coupling in the twisted WS_2/MoS_2 heterostructures. And at θ = 0°, 60°, or 120°, the interlayer mechanical coupling is the strongest and the interlayer distance is the shortest, in accordance with the previous reports [47, 48, 60]. In addition, as presented in Fig. 4(a), for the separation ($\omega_A - \omega_E$) of MoS_2, most of the orange dot points are below the red dashed lines, other than like WS_2 (Fig. 4(b)), of which the separations (represented by brown dot points) are always above the red dashed lines for all twist angles. This is due to the extra contribution from the doping-induced shifts in $A_{1g}(\Gamma)$ modes of MoS_2 and WS_2.

To further confirm the doping effect, we also analyze the $A_{1g}(\Gamma)$ mode linewidth (FWHM). As shown in Fig. 5, for the $A_{1g}(\Gamma)$ mode of MoS_2 in the twisted heterostructures, the FWHM is broader than that of pure monolayer MoS_2 and has

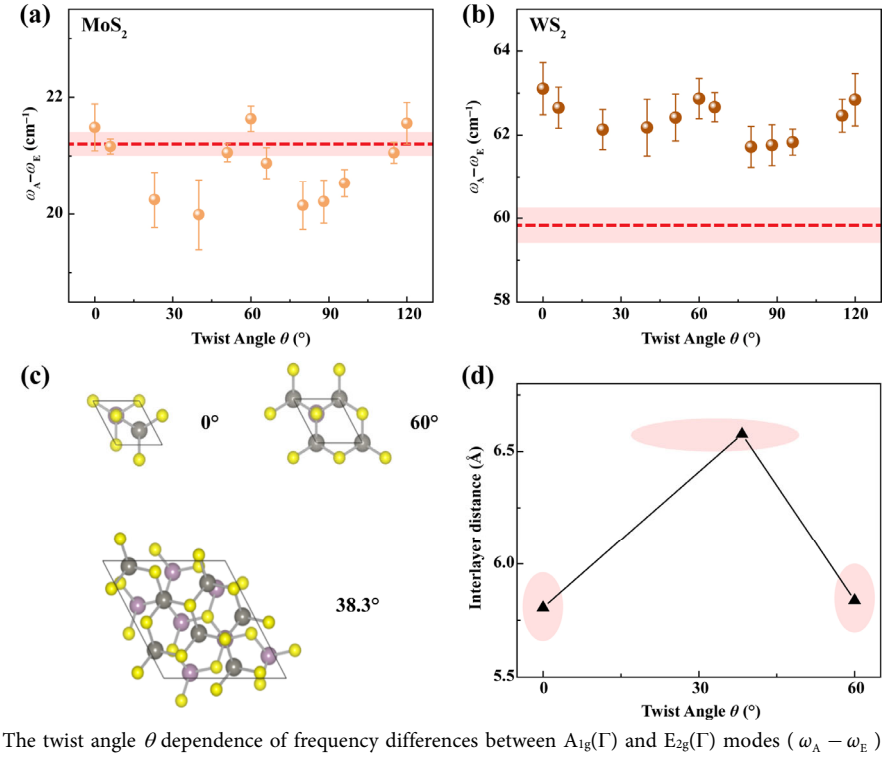

Figure 4 ((a) and (b)) The twist angle θ dependence of frequency differences between $A_{1g}(\Gamma)$ and $E_{2g}(\Gamma)$ modes ($\omega_A - \omega_E$) of MoS_2 (a) and WS_2 (b). ω_E and ω_A are taken from Figs. 3(b)–3(e), accordingly. The orange and brown dots correspond to the ($\omega_A - \omega_E$) of MoS_2 and WS_2 in the twisted heterostructures, respectively. The error bars are calculated through the propagation of uncertainty equation of $\sigma(\omega_A - \omega_E) = \sqrt{\sigma(\omega_A)^2 + \sigma(\omega_E)^2}$ (See the ESM). The red dashed lines and the shaded areas refer to the average value and uncertainty of ($\omega_A - \omega_E$) in the constituent layers, respectively. (c) Periodic unit cells at the twisted configurations of 0°, 60°, and 38.3° for theoretical calculations. (d) The calculated interlayer distance (between Mo and W atom layers) as a function of twist angle θ. Pink ovals are the guide for eyes.

a maximum upshift of about 1 cm^{-1} around 30° or 90° in comparison with either 0°, 60°, or 120°. (See Fig. 5(a)) The analogous variation of the linewidth of $A_{1g}(\Gamma)$ as a function of twist angle in WS_2 of the heterostructures is also displayed in Fig. 5(b). Figures 5(c) and 5(d) present the corresponding ascending or descending number sequence of $A_{1g}(\Gamma)$ FWHM in Figs. 5(a) and 5(b), respectively, which further reveal the distinct trend and difference. The pink and blue solid ellipses highlight the angles around 0°, 60°, or 120°, and around 30° or 90°, respectively. To explain the reasons behind the angle-dependent variation phenomena, we first need to consider the impacts on the linewidth of $A_{1g}(\Gamma)$ phonon mode. As we can see from the previous studies [19, 52, 54, 59, 61], the linewidth of $A_{1g}(\Gamma)$ mode is mainly affected by interlayer mechanical coupling, carrier doping and strain. The linewidth of $A_{1g}(\Gamma)$ mode can become narrower as the thickness of TMDs increases because of the enhanced interlayer mechanical coupling [19, 52, 53, 62]. For instance, with the thickness of WS_2 increasing from monolayer to bilayer, the $A_{1g}(\Gamma)$ mode linewidth undergoes a dramatic reduction by around 1 cm^{-1} [52]. Additionally, in an electrically gated monolayer TMD transistor, the electrical doping can also make the linewidth of $A_{1g}(\Gamma)$ mode broaden accordingly [59]. Although the tensile strain is able to broaden the $A_{1g}(\Gamma)$ mode as well [55, 57, 58], we do not take the strain effect into consideration of our case as mentioned before, because the $E_{2g}(\Gamma)$ modes are not found to become enlarged in the twisted heterostructures at the same time (See Fig. S2 in the ESM). Hence, we attribute the variable linewidths of $A_{1g}(\Gamma)$ modes in the twisted heterostructures to the combination effects of interlayer mechanical coupling and carrier doping.

In the case of the heterostructure, monolayer MoS_2 is interfaced with WS_2, forming a "bilayer-like" structure, where the $A_{1g}(\Gamma)$ modes can become narrower due to the enhanced interlayer mechanical coupling [19, 53]. In addition, in the twisted MoS_2/WS_2 heterostructures, the type-II band alignment was formed, in which, the electron (hole) transfers from WS_2 (MoS_2) to MoS_2 (WS_2). Thus, for MoS_2 in the twisted heterostructures, the broadening effect of $A_{1g}(\Gamma)$ mode was ascribed to the competing of increased interlayer mechanical coupling and electron doping, which means in the "bilayer" structure, the increased interlayer mechanical interaction is capable of reducing the linewidth of $A_{1g}(\Gamma)$ mode, whereas the electron doping extends the linewidth of $A_{1g}(\Gamma)$. Besides, in connection with Fig. 4(d), the similar trend of $A_{1g}(\Gamma)$ linewidth as a function of twist angle θ also implies that the interlayer coupling in the heterostructures with θ around 0°, 60°, or 120° is stronger than that with twist angle θ around 30° and 90°, as the interlayer distance of the twisted heterostructures around 0°, 60°, or 120° is comparatively shorter. Thus, the $A_{1g}(\Gamma)$ narrowing occurs in the heterostructures with twist angle θ around 0°, 60°, or 120°, accordingly. It should be noted that though the charge transfer may also vary with the twist angle, how the electron density originating from the charge transfer boosts the trends is not discussed in detail in this work, as the charge transfer is complicated in some twist angles (See the ESM for the detailed comparisons of electronic band structures between different twist angles). For the case of WS_2, the trend is not as obvious as that of MoS_2 and the linewidths of $A_{1g}(\Gamma)$ mode fluctuate across the standard deviation shadow line, as well. It is possibly caused by the following two reasons. First, the $A_{1g}(\Gamma)$ peak is very weak in the pristine WS_2, thus giving a relatively large standard deviation, which almost hinders the narrowing effect of $A_{1g}(\Gamma)$. Second, as discussed above, the little bit of *n*-doping induced by the charge transfer in WS_2 of the twisted heterostructures is expected to decrease the linewidth of $A_{1g}(\Gamma)$ mode, though it is just a plausible estimation, as the electron-phonon coupling of $A_{1g}(\Gamma)$ mode in monolayer WS_2 has not been determined yet.

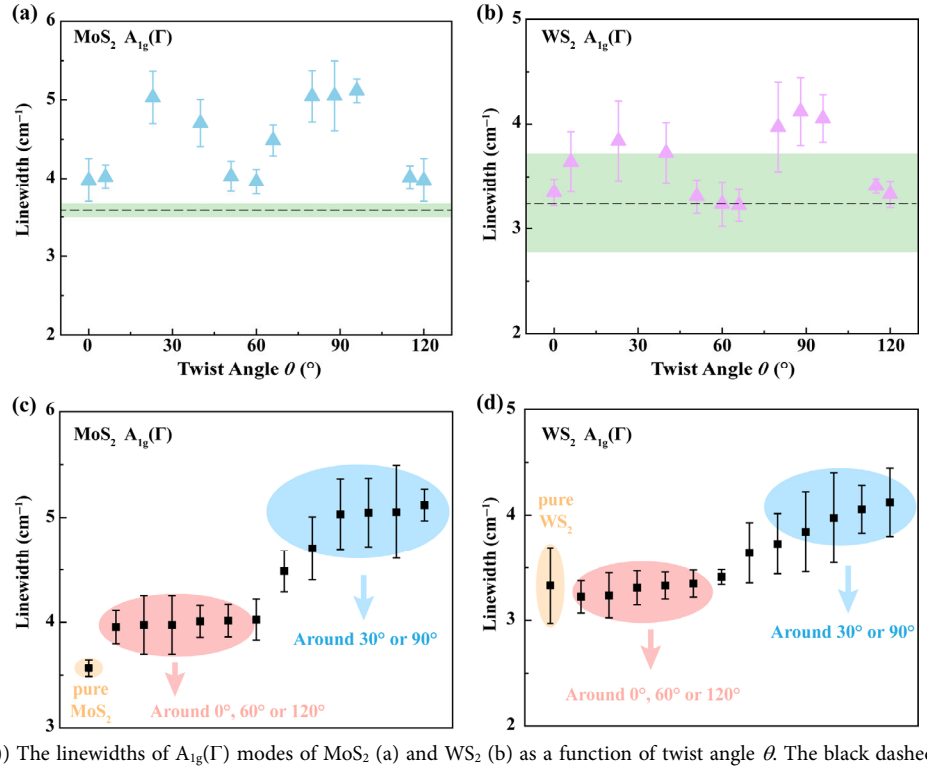

Figure 5 ((a) and (b)) The linewidths of $A_{1g}(\Gamma)$ modes of MoS_2 (a) and WS_2 (b) as a function of twist angle θ. The black dashed lines and the shaded areas represent the average linewidth and standard deviation of $A_{1g}(\Gamma)$ in the constituent layers, respectively. ((c) and (d)) The corresponding sort of $A_{1g}(\Gamma)$ linewidths from (a) and (b) in the descending or ascending sequence for (c) MoS_2 and (d) WS_2 of the twisted heterostructures, respectively. The pink and blue solid ovals highlight a group of data extracted from the samples with twist angles around 0°, 60°, or 120°, and around 30° or 90°, respectively. The orange solid oval highlights the data collected from pure monolayer samples.

In the twisted heterostructures of TMDs, both interlayer mechanical coupling and charge transfer effects contribute to the changes of Raman features, which is unlike the ones of most studied in homo-bilayer TMDs. In the twisted homostructures of TMDs, charge transfer effect is absent in the analysis of twist angle-dependent interlayer interactions since both layers of the homostructures own the same band structures. In our case, with the help of PL studies on the dominant negatively charged (X_A^-) and neutral (X_A) A exciton emissions, and theoretical calculations of the band alignment, the charge transfer between the heterostructures is further considered to clarify the Raman scattering modulations in addition to the interlayer mechanical coupling. More specifically, the in-plane $E_{2g}(\Gamma)$ modes of both MoS_2 and WS_2 layers obviously soften around θ = 0° and 60°, being similar with the ones of twisted homo-bilayer TMDs. However, distinct from the identical blueshift of $A_{1g}(\Gamma)$ mode in the twisted homo-bilayer TMDs [16, 19], the heterostructures of WS_2/MoS_2 present an enhanced redshift and a slight blueshift of the out-of-plane $A_{1g}(\Gamma)$ mode for MoS_2 and WS_2, respectively, which is explained in terms of the presence of interlayer charge transfer induced electron and hole doping in MoS_2 and WS_2, respectively.

3 Conclusions

To sum up, the interlayer mechanical coupling and charge transfer effects of twisted heterostructures of WS_2/MoS_2 have been investigated by micro-Raman spectroscopy. The type-II alignment of WS_2/MoS_2 is formed and the interlayer charge transfer occurs as evidenced by the evolution of PL emission components in each layer. Moreover, the periodic modulations of $E_{2g}(\Gamma)$ and $A_{1g}(\Gamma)$ modes have been revealed by measuring Raman scattering features of twisted heterostructures of WS_2/MoS_2. The changes of Raman peak separation ($\omega_A - \omega_E$) and $A_{1g}(\Gamma)$ linewidth have been correlated with interlayer mechanical coupling and charge transfer effects, where the interlayer mechanical coupling plays a dominant role in these variations of Raman modes. Our findings are significant for understanding how the twist angle affects the optical properties of vdWs TMD heterostructures, which are fundamentally important for developments of electronic and optoelectronic applications based on 2D vdWs heterostructures.

4 Methods

4.1 Growth of MoS_2 and WS_2

MoS_2 monolayers were grown on SiO_2/Si substrates by CVD method using MoO_3 and sulfur (Sigma Aldrich) as the reaction sources [33]. The synthesis process of MoS_2 was conducted in quartz tubes with the diameter of 1 inch under temperature ranging from 700 to 750 °C. The argon gas flowed in the tubes with the flowing rate of 80 sccm. A silicon boat containing 10 mg MoO_3 was put in the center of the tube. The SiO_2/Si substrate is placed on the boat with the surface downside. We also have another silicon boat with 0.5 g sulfur powder located on the upstream. For the synthesis procedure, the temperature first ramped up to 750 °C in 15 min, and then was kept at the reaction temperature for about 5–10 min, followed by the furnace cooling down to room temperature gradually.

Monolayer WS_2 was grown on sapphire by using the similar method that has been reported in our previous work [32]. The growth temperature is comparable to or slightly higher than that for monolayer WS_2 on SiO_2/Si substrates. Commercial sulfur and WO_3 powders (> 99.5%, Sigma Aldrich) and ultra-high purity argon flow of 300 sccm were used as the reaction sources and carrier gas, respectively.

4.2 Stacking of WS_2/MoS_2 heterostructures

WS_2 monolayers were detached from the sapphire substrates via a dry transfer method and then stacked onto MoS_2 monolayers with the help of home-made heterostructure transfer microscopic system. First, monolayer WS_2 on sapphires were spin-coated with PMMA (3% dissolved in tetrahydrofuran (THF)). Second, the PMMA film was baked at 175 °C for 30 s, followed by scratching off about 1 mm wide polymer strips at the edges of sapphires. Note that at least two neighboring edges have to be scratched, during which, the needful samples should avoid being damaged. Third, a PDMS polymer (Gel Pak, USA) pre-deposited on the quartz glass was used to cover the PMMA. Then, a small droplet of around 1 ml distilled water was put on the scratched film edges, followed by peeling off the PDMS. As a consequence, the PMMA associated with monolayer WS_2 was transferred onto the PDMS/glass due to the hydrophilic surface of sapphires. Forth, the PDMS/glass was subsequently mounted onto the micromanipulator, followed by the alignment through the optical microscopic system. After finishing the alignment, the WS_2/PMMA was transferred onto monolayer MoS_2 from the PDMS by means of heating at 80 °C. In the end, the PMMA was washed away by the acetone. To further remove the residues, the annealing of the samples was performed under the pressure of 10^{-5} mbar at 300 °C for 4 h. Optical images of WS_2/MoS_2 heterostructures with different twist angles are shown in Fig. S4 in the ESM.

4.3 Raman and PL characterizations

Raman and PL spectra were collected using a WITec Alpha300 series confocal microscopic system with a ×100 objective lens of NA = 0.95. An excitation laser of 532 nm (E_{laser} = 2.33 eV) is used, unless otherwise stated. The laser spot size is around 500 nm in diameter [37]. Before the measurements, the system was aligned well and calibrated with the Raman peak of Si at 520 cm^{-1}. We use 2,400 lines per mm grating for the collection of Raman spectra and a spectral resolution of 0.9 cm^{-1} obtained through monitoring the linewidth of the Mercury atomic emission line, was guaranteed [38]. The linewidths of Raman peaks were corrected through subtracting the extra broadening of 0.9 cm^{-1} from the fitted values. The laser power was kept less than 0.1 mW in order to prevent laser-induced heating effect on the samples. All the Raman spectra are normalized to the Si peak at 520 cm^{-1}.

4.4 Density functional theory calculations

We performed DFT calculations using the Vienna ab initio simulation package (VASP) program [63]. The local density approximation (LDA) functional was selected to treat the exchange-correlation interaction with the plane-wave cutoff energy of 500 eV. The semi-empirical correction scheme of Grimme (DFT-D2) was selected to evaluate the effects of vdWs interaction on the electronic properties of the MoS_2/WS_2 heterostructures [64]. Different MoS_2/WS_2 heterostructure configurations with twist angle θ equal to 0°, 38.3°, and 60° were constructed with a vacuum layer larger than 20 Å to avoid the interaction between periodic images along the c axis. The convergence condition for the energy was chosen as 10^{-6} eV, and the forces on each atom converged to within 0.01 eV/Å. The Monkhorst-Pack scheme was employed to sample the Brillouin zone with a mesh of 15 × 15 × 1 for the full relaxation and 25 × 25 × 1 for the self-consistent calculations of both 0° and 60° twisted MoS_2/WS_2 heterostructures, respectively, while it holds a mesh of 5 × 5 × 1 for 38.3° twisted one. The band

structures were calculated along the high-symmetry points using the path Γ-M-K-Γ by representing the states from MoS_2 and WS_2 with blue and red colors, respectively. Spatial maps of charge density difference for the MoS_2/WS_2 heterostructures were calculated by: $\rho = \rho(WS_2/MoS_2) - \rho(MoS_2) - \rho(WS_2)$, where $\rho(WS_2/MoS_2)$, $\rho(MoS_2)$, and $\rho(WS_2)$ are the charge density of the MoS_2/WS_2 heterostructure, pristine MoS_2 and WS_2, respectively. The blue (yellow) distribution represents charge depletion (accumulation). Note that the isosurface level is taken as 2.5×10^{-4} e/Å^3, and spin-orbit coupling was not involved in our calculations.

Acknowledgements

We thank Dr. Jiaxu Yan from Institute of Advanced Materials, Nanjing Tech. University and Dr. Juan Xia from University of Science and Technology, China for their helpful discussions. This work was mainly supported by the National Key R&D Program of China (Grant No. 2018YFA0703700) and the Ministry of Education, Singapore, MOE Tier 1 RG93/19, NRF-CRP-21-2018-0007, MOE2018-T2-2-072, and MOE2019-T2-1-004. C. X. C. also thanks the support of the National Natural Science Foundation of China (Grant No. 61774040), the Shanghai Municipal Science and Technology Commission (Grant No. 18JC1410300), the Fudan University-CIOMP Joint Fund (Grant No. FC2018-002), the National Young 1000 Talent Plan of China, and the Shanghai Municipal Natural Science Foundation (No. 16ZR1402500). J. Z. S. appreciates the support of the Fundamental Research Funds for the Central Universities of China, National Natural Science Foundation of China under Grant No. 61904151, Natural Science Foundation of Shaanxi under Grant No. 2020JM-108, and the Joint Research Funds of Department of Science & Technology of Shaanxi Province and Northwestern Polytechnical University (No. 2020GXLH-Z-020). Z. L. acknowledges the support of MOE Tier 1 grant RG164/15, Tier 2 grant MOE2016-T2-2-153, and MOE2015-T2-2-007, and Singapore National Research Foundation under NRF award No. NRF-NRFF2013-08. W. H. Y. acknowledges the support of the National Natural Science Foundations of China (Grant No. 61704040). This research was also supported by Zhejiang Provincial Natural Science Foundation of China (Grant No. LGG19F040003).

Electronic Supplementary Material: Supplementary material (further details of the variations of $A_{1g}(\Gamma)$ intensity and $E_{2g}(\Gamma)$ linewidth as a function of twist angle θ, the determination of uncertainties, DFT calculations of electronic band structures and optical images of WS_2/MoS_2 heterostructures with different twist angles) is available in the online version of this article at https://doi.org/10.1007/s12274-020-3193-y.

References

[1] Geim, A. K.; Grigorieva, I. V. Van der Waals heterostructures. *Nature* **2013**, *499*, 419–425.

[2] Wang, X. M.; Xia, F. N. Stacked 2D materials shed light. *Nat. Mater.* **2015**, *14*, 264–265.

[3] Mak, K. F.; Shan, J. Photonics and optoelectronics of 2D semiconductor transition metal dichalcogenides. *Nat. Photonics* **2016**, *10*, 216–226.

[4] Li, B.; Huang, L.; Zhong, M. Z.; Li, Y.; Wang, Y.; Li, J. B.; Wei, Z. M. Direct vapor phase growth and optoelectronic application of large band offset SnS_2/MoS_2 vertical bilayer heterostructures with high lattice mismatch. *Adv. Electron. Mater.* **2016**, *2*, 1600298.

[5] Sun, G. Z.; Li, B.; Wang, S. F.; Zhang, Z. W.; Li, J.; Duan, X. D.; Duan, X. F. Selective growth of wide band gap atomically thin Sb_2O_3 inorganic molecular crystal on WS_2. *Nano Res.* **2019**, *12*, 2781–2787.

[6] Li, H.; Wu, J.; Huang, X.; Yin, Z. Y.; Liu, J. Q.; Zhang, H. A universal, rapid method for clean transfer of nanostructures onto various substrates. *ACS Nano* **2014**, *8*, 6563–6570.

[7] Withers, F.; Del Pozo-Zamudio, O.; Mishchenko, A.; Rooney, A. P.; Gholinia, A.; Watanabe, K.; Taniguchi, T.; Haigh, S. J.; Geim, A. K.; Tartakovskii, A. I. et al. Light-emitting diodes by band-structure engineering in van der Waals heterostructures. *Nat. Mater.* **2015**, *14*, 301–306.

[8] Jin, C. H.; Regan, E. C.; Yan, A. M.; Utama, M. I. B.; Wang, D. Q.; Zhao, S. H.; Qin, Y.; Yang, S. J.; Zheng, Z. R.; Shi, S. Y. et al. Observation of moiré excitons in WSe_2/WS_2 heterostructure superlattices. *Nature* **2019**, *567*, 76–80.

[9] Seyler, K. L.; Rivera, P.; Yu, H. Y.; Wilson, N. P.; Ray, E. L.; Mandrus, D. G.; Yan, J. Q.; Yao, W.; Xu, X. D. Signatures of moiré-trapped valley excitons in $MoSe_2/WSe_2$ heterobilayers. *Nature* **2019**, *567*, 66–70.

[10] Tran, K.; Moody, G.; Wu, F. C.; Lu, X.B.; Choi, J.; Kim, K.; Rai, A.; Sanchez, D. A.; Quan, J. M.; Singh, A. et al. Evidence for moiré excitons in van der Waals heterostructures. *Nature* **2019**, *567*, 71–75.

[11] Alexeev, E. M.; Ruiz-Tijerina, D. A.; Danovich, M.; Hamer, M. J.; Terry, D. J.; Nayak, P. K.; Ahn, S.; Pak, S.; Lee, J.; Sohn, J. I. et al. Resonantly hybridized excitons in moiré superlattices in van der Waals heterostructures. *Nature* **2019**, *567*, 81–86.

[12] Chiu, M. H.; Li, M. Y.; Zhang, W. J.; Hsu, W. T.; Chang, W. H.; Terrones, M.; Terrones, H.; Li, L. J. Spectroscopic Signatures for Interlayer Coupling in MoS_2-WSe_2 van der Waals Stacking. *ACS Nano* **2014**, *8*, 9649–9656.

[13] Puretzky, A. A.; Liang, L. B.; Li, X. F.; Xiao, K.; Wang, K.; Mahjouri-Samani, M.; Basile, L.; Idrobo, J. C.; Sumpter, B. G.; Meunier, V. et al. Low-frequency Raman fingerprints of two-dimensional metal dichalcogenide layer stacking configurations. *ACS Nano* **2015**, *9*, 6333–6342.

[14] Lim, H.; Yoon, S. I.; Kim, G.; Jang, A. R.; Shin, H. S. Stacking of two-dimensional materials in lateral and vertical directions. *Chem. Mater.* **2014**, *26*, 4891–4903.

[15] Roy, T.; Tosun, M.; Cao, X.; Fang, H.; Lien, D. H.; Zhao, P.; Chen, Y. Z.; Chueh, Y. L.; Guo, J.; Javey, A. Dual-gated MoS_2/WSe_2 van der waals tunnel diodes and transistors. *ACS Nano* **2015**, *9*, 2071–2079.

[16] Van Der Zande, A. M.; Kunstmann, J.; Chernikov, A.; Chenet, D. A.; You, Y. M.; Zhang, X. X.; Huang, P. Y.; Berkelbach, T. C.; Wang, L.; Zhang, F. et al. Tailoring the electronic structure in bilayer molybdenum disulfide via interlayer twist. *Nano Lett.* **2014**, *14*, 3869–3875.

[17] Huang, S. X.; Liang, L. B.; Ling, X.; Puretzky, A. A.; Geohegan, D. B.; Sumpter, B. G.; Kong, J.; Meunier, V.; Dresselhaus, M. S. Low-frequency interlayer Raman modes to probe interface of twisted bilayer MoS_2. *Nano Lett.* **2016**, *16*, 1435–1444.

[18] Zheng, S. J.; Sun, L. F.; Zhou, X. H.; Liu, F. C.; Liu, Z.; Shen, Z. X.; Fan, H. J. Coupling and interlayer exciton in twist-stacked WS_2 bilayers. *Adv. Opt. Mater.* **2015**, *3*, 1600–1605.

[19] Liu, K. H.; Zhang, L. M.; Cao, T.; Jin, C. H.; Qiu, D. A.; Zhou, Q.; Zettl, A.; Yang, P. D.; Louie, S. G.; Wang, F. Evolution of interlayer coupling in twisted molybdenum disulfide bilayers. *Nat. Commun.* **2014**, *5*, 4966.

[20] Huang, S. X.; Ling, X.; Liang, L. B.; Kong, J.; Terrones, H.; Meunier, V.; Dresselhaus, M. S. Probing the interlayer coupling of twisted bilayer MoS_2 using photoluminescence spectroscopy. *Nano Lett.* **2014**, *14*, 5500–5508.

[21] Hong, X. P.; Kim, J.; Shi, S. F.; Zhang, Y.; Jin, C. H.; Sun, Y. H.; Tongay, S.; Wu, J. Q.; Zhang, Y. F.; Wang, F. Ultrafast charge transfer in atomically thin MoS_2/WS_2 heterostructures. *Nat. Nanotechnol.* **2014**, *9*, 682–686.

[22] Rigos, A. F.; Hill, H. M.; Li, Y. L.; Chernikov, A.; Heinz, T. F. Probing interlayer interactions in transition metal dichalcogenide heterostructures by optical spectroscopy: MoS_2/WS_2 and $MoSe_2/WSe_2$. *Nano Lett.* **2015**, *15*, 5033–5038.

[23] Zhang, J.; Hong, H.; Lian, C.; Ma, W.; Xu, X. Z.; Zhou, X.; Fu, H. X.; Liu, K. H.; Meng, S. Interlayer-state-coupling dependent ultrafast charge transfer in MoS_2/WS_2 Bilayers. *Adv. Sci.* **2017**, *4*, 1700086.

[24] Tongay, S.; Fan, W.; Kang, J.; Park, J.; Koldemir, U.; Suh, J.; Narang, D. S.; Liu, K.; Ji, J.; Li, J. B. et al. Tuning interlayer coupling in large-area heterostructures with CVD-Grown MoS_2 and WS_2 monolayers. *Nano Lett.* **2014**, *14*, 3185–3190.

[25] Zhou, H. Z.; Zhao, Y. D.; Zhu, H. M. Dielectric environment-robust ultrafast charge transfer between two atomic layers. *J. Phys. Chem. Lett.* **2019**, *10*, 150–155.

[26] Wang, K.; Huang, B.; Tian, M. K.; Ceballos, F.; Lin, M. W.; Mahjouri-Samani, M.; Boulesbaa, A.; Puretzky, A. A.; Rouleau, C. M.; Yoon, M. et al. Interlayer coupling in twisted WSe_2/WS_2 bilayer heterostructures revealed by optical spectroscopy. *ACS Nano* **2016**, *10*, 6612–6622.

[27] Ceballos, F.; Bellus, M. Z.; Chiu, H. Y.; Zhao, H. Ultrafast charge separation and indirect exciton formation in a MoS_2-$MoSe_2$ van der waals heterostructure. *ACS Nano* **2014**, *8*, 12717–12724.

[28] Rivera, P.; Schaibley, J. R.; Jones, A. M.; Ross, J. S.; Wu, S. F.; Aivazian, G.; Klement, P.; Seyler, K.; Clark, G.; Ghimire, N. J. et al. Observation of long-lived interlayer excitons in monolayer $MoSe_2$-WSe_2 heterostructures. *Nat. Commun.* **2015**, *6*, 6242.

[29] Gong, Y. J.; Lei, S. D.; Ye, G. L.; Li, B.; He, Y. M.; Keyshar, K.; Zhang, X.; Wang, Q. Z.; Lou, J.; Liu, Z. et al. Two-step growth of two-dimensional $WSe_2/MoSe_2$ heterostructures. *Nano Lett.* **2015**, *15*, 6135–6141.

[30] Huang, C. M.; Wu, S. F; Sanchez, A. M.; Peters, J. J. P.; Beanland, R.; Ross, J. S.; Rivera, P.; Yao, W.; Cobden, D. H.; Xu, X. D. Lateral heterojunctions within monolayer $MoSe_2$-WSe_2 semiconductors. *Nat. Mater.* **2014**, *13*, 1096–1101.

[31] Torun, E.; Miranda, H. P. C.; Molina-Sánchez, A.; Wirtz, L. Interlayer and intralayer excitons in MoS_2/WS_2 and $MoSe_2/WSe_2$ heterobilayers. *Phys. Rev. B* **2018**, *97*, 245427.

[32] Cong, C. X.; Shang, J. Z.; Wu, X.; Cao, B. C.; Peimyoo, N.; Qiu, C. Y.; Sun, L. T.; Yu, T. Synthesis and optical properties of large-area single-crystalline 2D semiconductor WS_2 monolayer from chemical vapor deposition. *Adv. Opt. Mater.* **2014**, *2*, 131–136.

[33] Zhou, J. D.; Lin, J. H.; Sims, H.; Jiang, C. Y.; Cong, C. X.; Brehm, J. A.; Zhang, Z. W.; Niu, L.; Chen, Y.; Zhou, Y. et al. Synthesis of Co-Doped MoS_2 monolayers with enhanced valley splitting. *Adv. Mater.* **2020**, *32*, 1906536.

[34] Feng, S.; Cong, C. X.; Peimyoo, N.; Chen, Y.; Shang, J. Z.; Zou, C. J.; Cao, B. C.; Wu, L. S.; Zhang, J.; Eginligil, M. et al. Tunable excitonic emission of monolayer WS_2 for the optical detection of DNA nucleobases. *Nano Res.* **2018**, *11*, 1744–1754.

[35] Liu, H. W.; Lu, J. P.; Ho, K.; Hu, Z. L.; Dang, Z. Y.; Carvalho, A.; Tan, H. R.; Tok, E. S.; Sow, C. H. Fluorescence concentric triangles: A case of chemical heterogeneity in WS_2 atomic monolayer. *Nano Lett.* **2016**, *16*, 5559–5567.

[36] Van Der Zande, A. M.; Huang, P. Y.; Chenet, D. A.; Berkelbach, T. C.; You, Y. M.; Lee, G. H.; Heinz, T. F.; Reichman, D. R.; Muller, D. A.; Hone, J. C. Grains and grain boundaries in highly crystalline monolayer molybdenum disulphide. *Nat. Mater.* **2013**, *12*, 554–561.

[37] Chen, Y.; Peng, B.; Cong, C. X.; Shang, J. Z.; Wu, L. S.; Yang, W. H.; Zhou, J. D.; Yu, P.; Zhang, H. B.; Wang, Y. L. et al. In-plane anisotropic thermal conductivity of few-layered transition metal dichalcogenide Td-WTe_2. *Adv. Mater.* **2019**, *31*, 1804979.

[38] Cong, C. X.; Yu, T. Enhanced ultra-low-frequency interlayer shear modes in folded graphene layers. *Nat. Commun.* **2014**, *5*, 4709.

[39] Gong, C.; Zhang, H. J.; Wang, W. H.; Colombo, L.; Wallace, R. M.; Cho, K. Band alignment of two-dimensional transition metal dichalcogenides: Application in tunnel field effect transistors. *Appl. Phys. Lett.* **2013**, *103*, 053513.

[40] Kang, J.; Tongay, S.; Zhou, J.; Li, J. B.; Wu, J. Q. Band offsets and heterostructures of two-dimensional semiconductors. *Appl. Phys. Lett.* **2013**, *102*, 012111.

[41] Mak, K. F.; He, K. L.; Lee, C.; Lee, G. H.; Hone, J.; Heinz, T. F.; Shan, J. Tightly bound trions in monolayer MoS_2. *Nat. Mater.* **2013**, *12*, 207–211.

[42] Mak, K. F.; He, K. L.; Shan, J.; Heinz, T. F. Control of valley polarization in monolayer MoS_2 by optical helicity. *Nat. Nanotechnol.* **2012**, *7*, 494–498.

[43] Feng, S.; Cong, C. X.; Konabe, S.; Zhang, J.; Shang, J. Z.; Chen, Y.; Zou, C. J.; Cao, B. C.; Wu, L. S.; Peimyoo, N. et al. Engineering valley polarization of monolayer WS_2: A physical doping approach. *Small* **2019**, *15*, 1805503.

[44] Shang, J. Z.; Shen, X. N.; Cong, C. X.; Peimyoo, N.; Cao, B. C.; Eginligil, M.; Yu, T. Observation of excitonic fine structure in a 2D transition-metal dichalcogenide semiconductor. *ACS Nano* **2015**, *9*, 647–655.

[45] Chen, H. L.; Wen, X. W.; Zhang, J.; Wu, T. M.; Gong, Y. J.; Zhang, X.; Yuan, J. T.; Yi, C. Y.; Lou, J.; Ajayan, P. M. et al. Ultrafast formation of interlayer hot excitons in atomically thin MoS_2/WS_2 heterostructures. *Nat. Commun.* **2016**, *7*, 12512.

[46] Mak, K. F.; Shan, J. Opportunities and challenges of interlayer exciton control and manipulation. *Nat. Nanotechnol.* **2018**, *13*, 974–976.

[47] Nayak, P. K.; Horbatenko, Y.; Ahn, S.; Kim, G.; Lee, J. U.; Ma, K. Y.; Jang, A. R.; Lim, H.; Kim, D.; Ryu, S. et al. Probing evolution of twist-angle-dependent interlayer excitons in $MoSe_2/WSe_2$ van der waals heterostructures. *ACS Nano* **2017**, *11*, 4041–4050.

[48] Okada, M.; Kutana, A.; Kureishi, Y.; Kobayashi, Y.; Saito, Y.; Saito, T.; Watanabe, K.; Taniguchi, T.; Gupta, S.; Miyata, Y. et al. Direct and indirect interlayer excitons in a van der waals heterostructure of hBN/WS_2/MoS_2/hBN. *ACS Nano* **2018**, *12*, 2498–2505.

[49] Gong, Y. J.; Lin, J. H.; Wang, X. L.; Shi, G.; Lei, S. D.; Lin, Z.; Zou, X. L.; Ye, G. L.; Vajtai, R.; Yakobson, B. I. et al. Vertical and in-plane heterostructures from WS_2/MoS_2 monolayers. *Nat. Mater.* **2014**, *13*, 1135–1142.

[50] Lin, Y. X.; Ling, X.; Yu, L. L.; Huang, S. X.; Hsu, A. L.; Lee, Y. H.; Kong, J.; Dresselhaus, M. S.; Palacios, T. Dielectric screening of excitons and trions in single-layer MoS_2. *Nano Lett.* **2014**, *14*, 5569–5576.

[51] Mak, K. F.; Lee, C.; Hone, J.; Shan, J.; Heinz, T. F. Atomically thin MoS_2: A new direct-gap semiconductor. *Phys. Rev. Lett.* **2010**, *105*, 136805.

[52] Zhao, W. J.; Ghorannevis, Z.; Amara, K. K.; Pang, J. R.; Toh, M.; Zhang, X.; Kloc, C.; Tan, P. H.; Eda, G. Lattice dynamics in mono- and few-layer sheets of WS_2 and WSe_2. *Nanoscale* **2013**, *5*, 9677–9683.

[53] Lee, C.; Yan, H.; Brus, L. E.; Heinz, T. F.; Hone, J.; Ryu, S. Anomalous lattice vibrations of single- and few-layer MoS_2. *ACS Nano* **2010**, *4*, 2695–2700.

[54] Dadgar, A. M.; Scullion, D.; Kang, K.; Esposito, D.; Yang, E. H.; Herman, I. P.; Pimenta, M. A.; Santos, E. J. G.; Pasupathy, A. N. Strain engineering and Raman spectroscopy of monolayer transition metal dichalcogenides. *Chem. Mater.* **2018**, *30*, 5148–5155.

[55] Wang, Y. L.; Cong, C. X.; Qiu, C. Y.; Yu, T. Raman spectroscopy study of lattice vibration and crystallographic orientation of monolayer MoS_2 under uniaxial strain. *Small* **2013**, *9*, 2857–2861.

[56] Molina-Sánchez, A.; Wirtz, L. Phonons in single-layer and few-layer MoS_2 and WS_2. *Phys. Rev. B* **2011**, *84*, 155413.

[57] Rice, C.; Young, R. J.; Zan, R.; Bangert, U.; Wolverson, D.; Georgiou, T.; Jalil, R.; Novoselov, K. S. Raman-scattering measurements and first-principles calculations of strain-induced phonon shifts in monolayer MoS_2. *Phys. Rev. B* **2013**, *87*, 081307.

[58] Zhang, X.; Qiao, X. F.; Shi, W.; Wu, J. B.; Jiang, D. S.; Tan, P. H. Phonon and Raman scattering of two-dimensional transition metal dichalcogenides from monolayer, multilayer to bulk material. *Chem. Soc. Rev.* **2015**, *44*, 2757–2785.

[59] Chakraborty, B.; Bera, A.; Muthu, D. V. S.; Bhowmick, S.; Waghmare, U. V.; Sood, A. K. Symmetry-dependent phonon renormalization in monolayer MoS_2 transistor. *Phys. Rev. B* **2012**, *85*, 161403.

[60] Zhang, J.; Wang, J. H.; Chen, P.; Sun, Y.; Wu, S.; Jia, Z. Y.; Lu, X. B.; Yu, H.; Chen, W.; Zhu, J. Q. et al. Observation of Strong Interlayer Coupling in MoS_2/WS_2 Heterostructures. *Adv. Mater.* **2016**, *28*, 1950–1956.

[61] Wang, Y. L.; Cong, C. X.; Yang, W. H.; Shang, J. Z.; Peimyoo, N.; Chen, Y.; Kang, J. Y.; Wang, J. P.; Huang, W.; Yu, T. Strain-induced direct–indirect bandgap transition and phonon modulation in monolayer WS_2. *Nano Res.* **2015**, *8*, 2562–2572.

[62] Saito, R.; Tatsumi, Y.; Huang, S.; Ling, X.; Dresselhaus, M. S. Raman spectroscopy of transition metal dichalcogenides. *J. Phys. Condens. Matter* **2016**, *28*, 353002.

[63] Kresse, G.; Hafner, J. *Ab initio* molecular dynamics for liquid metals. *Phys. Rev. B* **1993**, *47*, 558–561.

[64] Grimme, S. Semiempirical GGA-type density functional constructed with a long-range dispersion correction. *J. Comput. Chem.* **2006**, *27*, 1787–1799.